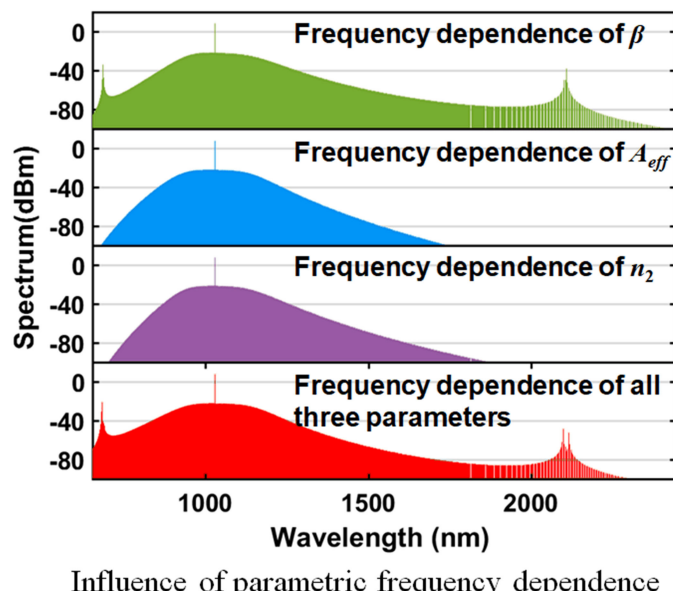


Numerical Investigation of Parametric Frequency Dependence in the Modeling of Octave-Spanning Kerr Frequency Combs

Volume 12, Number 2, April 2020

Yanjing Zhao
Liao Chen
Hao Hu
Chi Zhang
Xinliang Zhang



DOI: 10.1109/JPHOT.2020.2976558

Numerical Investigation of Parametric Frequency Dependence in the Modeling of Octave-Spanning Kerr Frequency Combs

Yanjing Zhao , Liao Chen , Hao Hu, Chi Zhang ,
and Xinliang Zhang 

Wuhan National Laboratory for Optoelectronics & School of Optical And Electronic Information, Huazhong University of Science and Technology, Wuhan 430074, China

DOI:10.1109/JPHOT.2020.2976558

This work is licensed under a Creative Commons Attribution 4.0 License. For more information, see <http://creativecommons.org/licenses/by/4.0/>

Manuscript received December 24, 2019; revised February 8, 2020; accepted February 23, 2020. Date of publication February 27, 2020; date of current version March 13, 2020. This work was supported by in part by National Science Foundation of China under Grants 61735006 and 61927817, and in part by China Postdoctoral Science Foundation under Grant 2018M640692. Corresponding author: Liao Chen (e-mail: liaochenchina@hust.edu.cn).

Abstract: A generalized Lugiato-Lefever equation in frequency domain for the modeling of Kerr frequency combs, including full-order frequency dependence of all parameters, is derived and solved without sacrifice of computational time. The proposed model shows high accuracy and efficiency in simulations, agreeing well with previous reports. Based on the proposed model, the influence of parametric frequency dependence is systematically investigated by generating octave-spanning combs in a silicon-nitride micro-ring-resonator with an air slot. The device is dispersion-tailored for broadband comb generation, and its parameters are strongly dependent on frequency. When considering three kinds of parametric influence separately, we reach the following conclusions. The frequency dependent propagation constant determines whether the dispersive wave is generated, matching well with the phase-matching condition. Besides, the frequency dependence of effective area and nonlinear refractive index can both introduce spectral blue-shift. Combining full-order frequency dependence of the three parameters together, a dispersive wave sideband emerges and this phenomenon has never been reported. Our work reveals that full-order frequency dependence of all parameters can be considered with high computational efficiency, which enables precise prediction of dispersive wave frequency for f-2f self-referencing and opens up more reliable avenues for the understanding of Kerr frequency comb generation, especially octave-spanning cases.

Index Terms: Frequency combs, solitons, kerr effect.

1. Introduction

Given the features as low cost, little energy consumption and compact footprint, Kerr frequency combs (also called micro-combs [1]) are promising to take frequency comb technology outside the laboratory. Among all the remarkable progress in the field over recent years, self-referenced micro-combs [2] have emerged as a milestone, which phase coherently link radio frequency to optical domain. This property makes them versatile precision tools for numerous applications, such as optical atomic clocks [3], precision spectroscopy [4] and astrophysical spectrometer calibration [5]. Generally, full-octave optical bandwidth is indispensable for frequency comb stabilization by f-2f self-referencing, which is traditionally explored by nonlinear spectral broadening of narrowband

micro-combs [6], [7]. Alternatively, dissipative Kerr solitons (i.e., stable temporal patterns in the cavity [8]) with dispersive waves [9] could provide octave-spanning spectra directly [10], making further integration of self-referenced micro-comb sources possible. As the spectral bandwidth is primarily determined by the cavity's dispersion, plenty of efforts have been paid to the dispersion engineering. Despite the strip waveguide structures initially [11], strip/slot waveguide structures [12], [13] are proposed to achieve flat anomalous dispersion profile more effectively. Most works above simulate octave-spanning comb generation by the Lugiato-Lefever equation in time domain (LLE-TD) [14]–[16], which is efficient but usually only contains the lower-order dispersion (namely lower-order frequency dependence of propagation constant). Although the modal expansion theory can efficiently include frequency dependent absorption coefficient and coupling coefficient [17], when the frequency dependence of nonlinear coefficient is further incorporated, the number of four-wave-mixing (FWM) coupling terms scales cubically with number of modes, limiting the model to narrowband cases [18]. As cavity parameters are strongly dependent on frequency for octave-spanning combs, the LLE-TD is modified to include frequency dependence of only specific parameters. The full-order dispersion (namely frequency dependence of propagation constant) is considered upon the proposal of LLE-TD [14]. Besides, the frequency dependent effective area is introduced as a self-steepening term [19], but it is only a first-order correction (linear approximation). Furthermore, the LLE-TD is simply Fourier transformed to contain more parametric frequency dependence [20], while numerous complicated convolutions exist, making it complex and time-consuming for simulations. Therefore, an efficient model is desired to systematically incorporate full-order frequency dependence of all parameters in the modeling of micro-comb generation, especially the octave-spanning ones.

In this article, the Lugiato-Lefever equation in frequency domain (LLE-FD) is deduced to include full-order frequency dependence of all parameters while maintaining high computational efficiency. The proposed LLE-FD is different from the simple Fourier transform of LLE-TD mentioned above. When only frequency dependence of propagation constant is considered, the LLE-FD is validated to be equivalent to LLE-TD. Simulations show excellent agreements with reported results [21]. Besides, the LLE-FD is comparable to LLE-TD in computational time and even more efficient for high precision solutions. To investigate the importance of parametric frequency dependence for octave-spanning combs with the proposed LLE-FD, a silicon nitride (SiN) micro-ring-resonator with an air slot is dispersion-tailored to generate broadband combs numerically. The investigation results could be concluded as below. The frequency dependent propagation constant will determine whether the dispersive wave is generated, while the frequency dependence of effective area and nonlinear refractive index can both induce spectral blue-shift. With full-order frequency dependence of all three parameters together, a new sideband except for dispersive waves is generated by degenerate FWM between a dispersive wave with pump. Our work enables precise prediction of dispersive wave frequency for self-referencing and paves valuable ways for the understanding of octave-spanning micro-combs.

2. Principle

Essentially, the LLE-TD is a variant of generalized nonlinear Schrodinger equation in time domain (GNLSE-TD) with merely frequency dependence of propagation constant. To include all parametric frequency dependence, the generalized nonlinear Schrodinger equation in frequency domain (GNLSE-FD) [22] is proposed and already applied to the supercontinuum [23].

$$\frac{\partial \tilde{C}(z, \omega)}{\partial z} + \frac{\alpha_i(\omega)}{2} \tilde{C}(z, \omega) - i[\beta(\omega) - \beta(\omega_0) - \beta_1(\omega_0)(\omega - \omega_0)] \tilde{C}(z, \omega) = i\gamma(\omega) \mathcal{F}\{|C(z, \tau)|^2 C(z, \tau)\}, \quad (1)$$

Here, ω is frequency, ω_0 is pump frequency, z is propagation distance, τ is time, $\alpha_i(\omega)$ is linear loss, $\beta_k(\omega_0)$ is the k th-order dispersion coefficient at pump frequency and $\beta(\omega)$ is propagation constant. $\tilde{C}(z, \omega)$ is the Fourier transform of $C(z, \tau)$, which is related to Fourier transform of intracavity field $E(z, \tau)$ by $\mathcal{F}\{C(z, \tau)\} = \tilde{C}(z, \omega) = [A_{\text{eff}}(\omega)/A_{\text{eff}}(\omega_0)]^{-1/4} \tilde{E}(z, \omega)$. The effective area $A_{\text{eff}}(\omega)$ and

nonlinear coefficient $\gamma(\omega)$ are given by [24]

$$A_{\text{eff}}(\omega) = \frac{\left(\int \int_{-\infty}^{+\infty} |F(x, y, \omega)|^2 dx dy \right)^2}{\int \int_{-\infty}^{+\infty} |F(x, y, \omega)|^4 dx dy}, \quad (2)$$

$$\gamma(\omega) = \frac{2\pi}{\lambda} \frac{\int \int_{-\infty}^{+\infty} n_2(x, y, \omega) |F(x, y, \omega)|^4 dx dy}{\left(\int \int_{-\infty}^{+\infty} |F(x, y, \omega)|^2 dx dy \right)^2}, \quad (3)$$

with $F(x, y, \omega)$ field profile, $n_2(x, y, \omega)$ nonlinear refractive index and λ wavelength. It is noteworthy that the GNLSE-FD is not the simple Fourier transform of GNLSE-TD, but originates from the Maxwell equations and just has similar form to GNLSE-TD after complex derivations [22].

Different from supercontinuums mainly obtained in straight waveguides, the micro-comb generation is also subjected to the cavity's boundary condition. The intracavity field at the beginning of $(m + 1)$ th roundtrip is related to that at the end of m th roundtrip:

$$E^{m+1}(0, \omega) = \sqrt{\theta(\omega)} E_{in}(\omega) + \sqrt{1 - \theta(\omega)} E^m(L, \omega) e^{i\phi_0}, \quad (4)$$

where $\theta(\omega)$ is coupling coefficient, $E_{in}(\omega)$ is continuous-wave (CW) pump amplitude, L is roundtrip length of the cavity and ϕ_0 is accumulated roundtrip linear phase.

Combining GNLSE-FD with the cavity's boundary condition, we obtain the LLE-FD which includes full-order frequency dependence of all parameters (here only Kerr effect is considered in nonlinear effects for simplification):

$$t_R \frac{\partial \tilde{C}(t, \omega)}{\partial t} + \left[\frac{\alpha_i(\omega) + \theta(\omega)}{2} + i\delta_0 \right] \tilde{C}(t, \omega) - iL[\beta(\omega) - \beta(\omega_0) - \beta_1(\omega_0)(\omega - \omega_0)] \tilde{C}(t, \omega) - \sqrt{\theta(\omega)} \tilde{C}_{in}(\omega) = i\gamma(\omega) L \cdot \mathcal{F} \left\{ |C(t, \tau)|^2 C(t, \tau) \right\}, \quad (5)$$

where t is slow time with respect to consecutive roundtrips, t_R is roundtrip time. The phase detuning parameter is $\delta_0 = 2\pi l \cdot \phi_0$ with l the order of cavity resonant mode closest to pump. $\tilde{C}_{in}(\omega)$ is related to CW pump $\tilde{E}_{in}(\omega)$ with similar transformation of $\tilde{C}(t, \omega)$. In contrast to the simple Fourier transformation of LLE-TD [20], the LLE-FD (combined by GNLSE-FD and cavity's boundary condition) avoids complicated convolution terms.

For clear comparison with LLE-FD, the traditional LLE-TD [14] is also written as

$$t_R \frac{\partial E(t, \tau)}{\partial t} = \left[-\frac{\alpha_{i0} + \theta_0}{2} - i\delta_0 + iL \sum_{k \geq 2} \frac{\beta_k}{k!} \left(i \frac{\partial}{\partial \tau} \right)^k + i\gamma_0 L |E(t, \tau)|^2 \right] E(t, \tau) + \sqrt{\theta_0} E_{in}, \quad (6)$$

here the parameters represent values at pump frequency like $\gamma_0 = \gamma(\omega_0)$. Compared with LLE-TD, the LLE-FD can natively include full-order frequency dependence of all parameters, such as the cavity loss, propagation constant, effective area, nonlinear refractive index and coupling coefficient. Notably the LLE-FD degenerates into LLE-TD when only propagation constant is frequency dependent. To solve the models, the fourth-order Runge-Kutta method is applied with adaptive step size method — local error method, which is detailed in Ref. [25].

3. Results

3.1 Accuracy and Efficiency Validation

To verify the accuracy of LLE-FD, we only consider the lower-order dispersion and use different simulation parameters in Ref. [21] for comparison. In situation A ($\beta_2 = -20 \text{ ps}^2/\text{km}$, $\beta_3 = 0.4 \text{ ps}^3/\text{km}$ and $\beta_4 = -8 \times 10^{-3} \text{ ps}^4/\text{km}$), the results of single soliton are obtained by LLE-FD, showing smooth spectral and temporal envelopes in Figs. 1(a, b). Instead for situation B ($\beta_2 = -20 \text{ ps}^2/\text{km}$, $\beta_3 = 0.4 \text{ ps}^3/\text{km}$ but $\beta_4 = 8 \times 10^{-3} \text{ ps}^4/\text{km}$), two dispersive waves are generated in spectrum, incurring temporal oscillations aside soliton pulses, as depicted in Figs. 1(e, f). For unambiguous

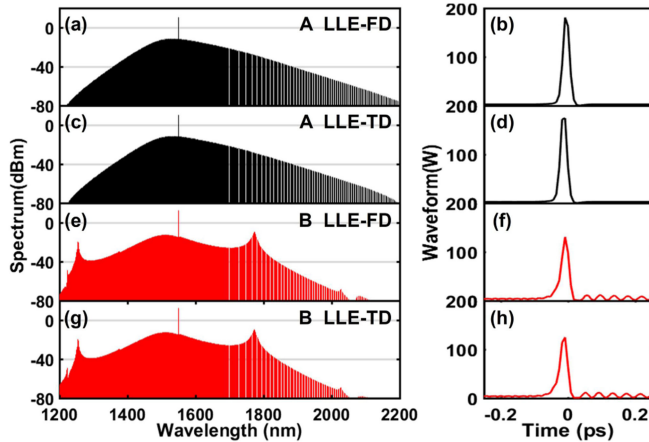


Fig. 1. Simulated results of single solitons by (a, b, e, f) LLE-FD, (c, d, g, h) LLE-TD. A and B represent two different anomalous dispersion parameters.

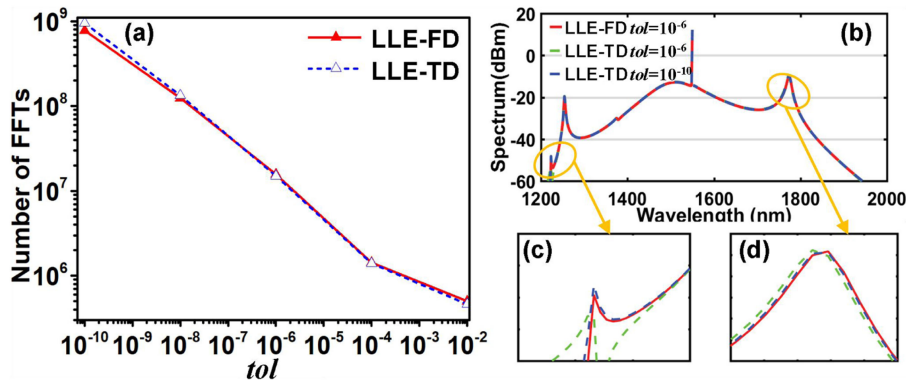


Fig. 2. (a) Global error of local error method versus number of FFTs in LLE-FD and LLE-TD; (b) comparison of spectral envelopes in three different conditions: red curve, results by LLE-FD with $tol = 10^{-6}$; green curve, results by LLE-TD with $tol = 10^{-6}$; blue curve, results by LLE-TD with $tol = 10^{-10}$; (c, d) enlarged drawings of (b).

comparison, numerical results by LLE-TD are also presented in Figs. 1(c, d, g, h), matching well with those by LLE-FD in two different dispersion conditions. Simulation results show great accordance with the phenomena in Ref. [21]. Consequently, it is validated again in simulation that LLE-TD is the particular case of LLE-FD with only lower-order dispersion considered.

Then the efficiencies of LLE-FD and LLE-TD are assessed in situation B using local error method without other parametric frequency dependence considered. The global error is the essential criteria in local error method and is defined as [25]:

$$tol = \frac{\|\tilde{C}_{coarse} - \tilde{C}_{fine}\|}{\|\tilde{C}_{fine}\|}, \quad (7)$$

where $\|\tilde{C}\| = (\int |\tilde{C}(\omega)|^2 d\omega)^{1/2}$, \tilde{C}_{coarse} is intracavity field simulated by step h , and \tilde{C}_{fine} is that by step $h/2$. The number of fast Fourier transforms (FFTs) is used to assess computational time [25], [26]. When the global error decreases, more precise solutions are obtained, with the price of increased FFTs. Fig. 2(a) illustrates the efficiencies of LLE-FD and LLE-TD, respectively. Both models show comparable performances for $tol \geq 10^{-6}$. Then with the precision improved (global

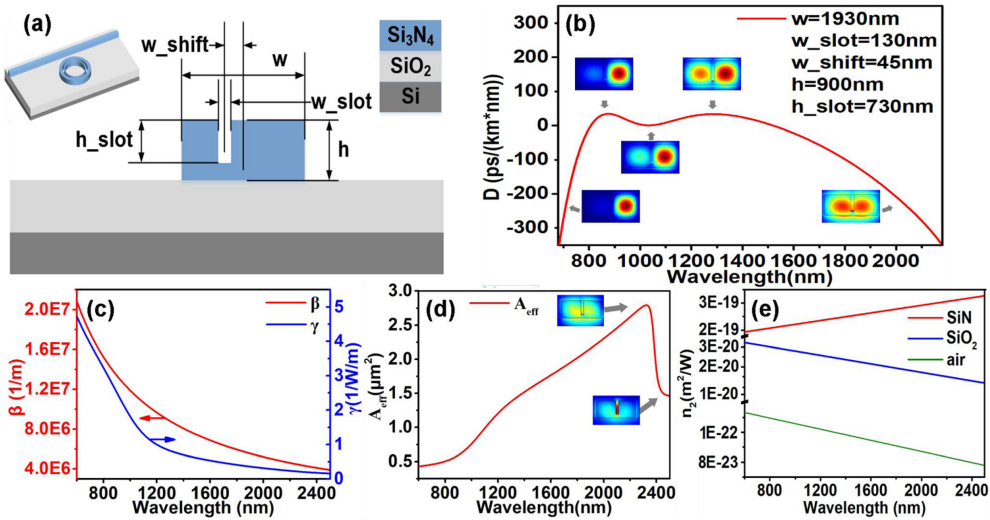


Fig. 3. Information of the dispersion-tailored micro-ring-resonator with an air slot. (a) Schematic and cross-section; (b) fundamental mode evolution and group velocity dispersion parameter profile; (c) the frequency dependence of propagation constant β and nonlinear coefficient γ ; (d) the frequency dependence of effective area A_{eff} , the insets show the mode profiles; (e) the frequency dependence of nonlinear refractive index n_2 .

error decreased), the advantage of LLE-FD gradually emerges. In the condition of $\text{tol} = 10^{-10}$, the LLE-TD takes 5.38 hours while LLE-FD allows for a time reduction of 1.45 hours.

For further validation of high efficiency in LLE-FD, single soliton spectra are simulated with $\text{tol} = 10^{-6}$ by both models, and shown as the red (LLE-FD) and green (LLE-TD) curves in Fig. 2(b). While most of the spectral information is in good agreement, there are indeed deviations at spectral wings (magnified in Figs. 2(c-d)), which are incurred by different numerical errors in the two models. To further improve the precision of solutions in LLE-TD, the spectrum is recalculated with $\text{tol} = 10^{-10}$. Apparently, the spectrum by LLE-FD with $\text{tol} = 10^{-6}$ (red curve) is consistent with that by LLE-TD with $\text{tol} = 10^{-10}$ (blue curve), however the FFTs number of the former is two-orders of magnitude smaller. Namely, for the same given global error, results of LLE-FD possess higher absolute accuracy than LLE-TD.

3.2 Parametric Frequency Dependence Investigation

3.2.1 Device Design: Moreover, to investigate influences of parametric frequency dependence for broadband micro-combs by LLE-FD, a SiN micro-ring-resonator with an air slot is carefully designed. Fig. 3(a) shows the schematic and cross section of the device. The w , h , w_{slot} , h_{slot} and w_{shift} are the waveguide width, waveguide height, slot width, slot height and slot offset from the waveguide center, respectively. With the wavelength increases, the power distribution of fundamental mode transits from the right side of the waveguide to the whole. This mode coupling improves the overall dispersion profile, since it induces an anti-crossing effect which brings in additional negative waveguide dispersion along a wide wavelength range [12]. With the optimized structure ($w = 1930$ nm, $w_{\text{slot}} = 130$ nm, $w_{\text{shift}} = 45$ nm, $h = 900$ nm, $h_{\text{slot}} = 730$ nm and radius $r = 100$ μm), we can achieve relatively flat anomalous dispersion curve in Fig. 3(b). Within the bandwidth of 722 nm, the dispersion value ranges from 0 to 33 ps/(nm·km) with three zero-dispersion wavelengths locating at 806 nm, 1030 nm and 1528 nm. Based on the specially designed device, it is expected to acquire octave-spanning comb generation.

For the designed device, the propagation constant $\beta(\omega)$, nonlinear coefficient $\gamma(\omega)$ and effective area $A_{\text{eff}}(\omega)$ are calculated by the finite element method. These parameters show significant frequency dependence in Figs. 3(c, d), which deviates greatly from previously assumed linear

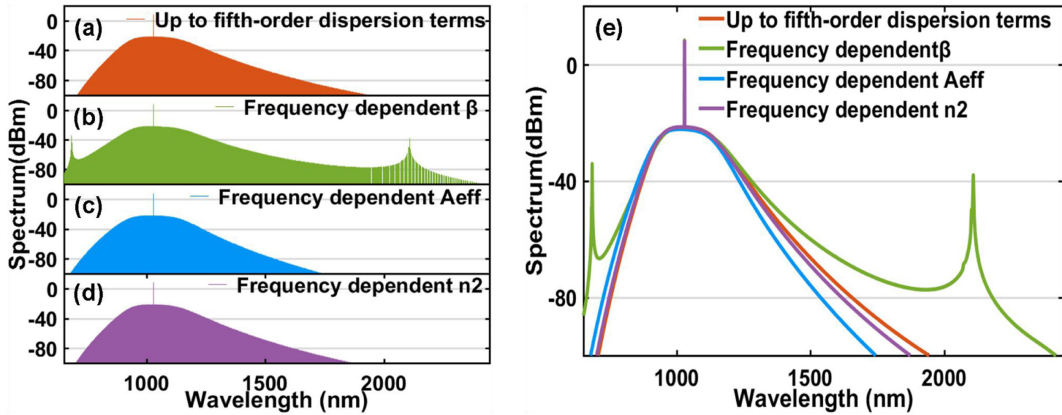


Fig. 4. Influence of parametric frequency dependence separately. Single soliton spectra with (a) only lower-order dispersion (up to fifth-order) included, (b) only frequency dependent propagation constant (namely, full-order dispersion) included, (c) only frequency dependent effective area included, (d) only frequency dependent nonlinear refractive index included; (e) comparison of the four spectral envelopes in (a–d). Here, $t_R = 4.45$ ps, $\alpha_i = \theta = 0.009$, $L = 628.32$ μm , $\delta_0 = 0.088$, $\beta_2 = -0.27$ ps^2/km , $\beta_3 = 1.88 \times 10^{-3}$ ps^3/km , $\beta_4 = -8.18 \times 10^{-4}$ ps^4/km , $\beta_5 = 7.13 \times 10^{-7}$ ps^5/km , $\gamma_0 = 1902.96$ $\text{W}^{-1}\text{km}^{-1}$, $A_{eff,0} = 0.83$ μm^2 , $tol = 1 \times 10^{-6}$.

relation [19]. The nonlinear coefficient is relevant with both effective area and nonlinear refractive index $n_2(\omega)$. However, nonlinear refractive index is scarcely measured, with values only available at specific wavelengths. As a proof-of-concept investigation, nonlinear refractive indexes of SiN, SiO_2 and air are estimated by linear fitting of the values obtained at two different wavelengths [27]–[29], illustrated in Fig. 3(e). With the wavelength increases, the guided mode gradually leaks into the slot and substrate, where nonlinear and linear refractive index $n(\omega)$ are smaller. Thus, the effective area increases, while propagation constant and nonlinear coefficient decrease correspondingly. For wavelength longer than 2330 nm, the fundamental mode transits from high index waveguide to air slot, leading to the sharp decrease in the effective area.

When only lower-order dispersion is concerned, numerical result is obtained by LLE-FD, with pump wavelength set at the zero-dispersion wavelength 1030 nm and pump power as 1 W. The lower-order dispersion is expanded up to fifth-order here ($\beta_2 = -0.27$ ps^2/km , $\beta_3 = 1.88 \times 10^{-3}$ ps^3/km , $\beta_4 = -8.18 \times 10^{-4}$ ps^4/km , $\beta_5 = 7.13 \times 10^{-7}$ ps^5/km), which is the general case in LLE-TD simulations [21], [30]. With optimized dispersion parameters, the single soliton spectrum covers nearly an octave with no dispersive waves in Fig. 4(a). The phase matching condition for dispersive wave generation is simplified as $\Delta\delta = \sum_{k=2}^5 \beta_k(\omega - \omega_0)^k/k! - \gamma P_s/2$, where P_s is the peak power of solitons [24]. Dispersive waves are induced when frequencies satisfy $\Delta\delta = 0$. According to the phase matching condition (blue curve in Fig. 5(a)), there is no zeros, consisting with the simulation results. Currently, the general modeling of octave-spanning micro-combs has been implemented this way with only lower-order dispersion considered.

3.2.2 Parametric Frequency Dependence: Finally, influences of the propagation constant, effective area and nonlinear refractive index are investigated separately based on the optimized device and LLE-FD. The propagation constant is connected with the effective refractive index $n_{eff}(\omega)$ by $\beta(\omega) = 2\pi n_{eff}(\omega)/\lambda$, reflecting the influence of full-order dispersion. The frequency dependence of propagation constant introduces variations to phase matching condition, incurring the generation of two dispersive waves and feeding the spectrum to normal dispersion regions in Fig. 4(b). Then the frequency dependence of effective area and nonlinear refractive index is investigated and shown in Fig. 4(c) and 4(d), respectively. Both parameters influence the spectral intensity distribution. For clear comparison, the spectral envelopes of the four conditions (in Figs. 4(a, b, c, d)) are illustrated in Fig. 4(e). Compared with the red curve when only lower-order dispersion is considered (general cases in LLE-TD), the frequency dependence of effective area (blue curve)

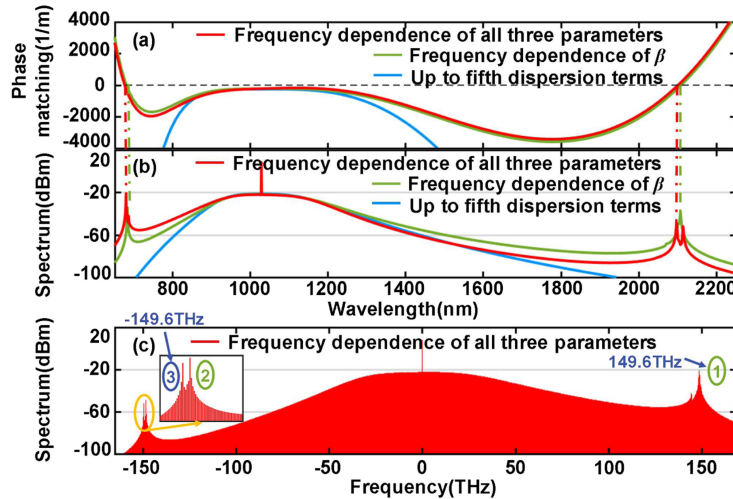


Fig. 5. (a) The phase matching condition for dispersive wave generation, (b) single soliton spectra, with only lower-order dispersion (blue curves), only frequency dependent propagation constant (green curves) and all three parametric frequency dependence (red curves); (c) single soliton spectrum in frequency domain with all three parametric frequency dependence, marked numbers represent spectral peaks except for pump.

and nonlinear refractive index (purple curve) is both proved to induce spectral blue-shift, while the former has greater influence. The smaller effective area at shorter wavelength leads to the increase of nonlinear coefficient, enhancing the FWM efficiency and spectral intensity. Results perform similarly with the wavelength increases. For wavelength longer than 2330 nm, though the effective area drops sharply, the spectrum is too weak to reflect its impact. As for the nonlinear refractive index, the influence of SiN material is dominant, because the guided mode is mainly restricted in this high index waveguide. According to Eq. (3), the nonlinear coefficient is proportional to the nonlinear refractive index. Thus, with the wavelength increases, the larger nonlinear refractive index of SiN material induces increased nonlinear coefficient, which ultimately enhances the spectral intensity. Therefore, the three kinds of parametric frequency dependence all affect spectral intensity distribution, while the frequency dependence of effective area and nonlinear refractive index could deterministically induce spectral blue-shift. Besides, the dispersive wave generation is only determined by frequency related propagation constant.

As mentioned above, two dispersive waves emerge at 685 nm and 2108 nm with only frequency dependence of propagation constant introduced. For full-order dispersion considered here, the phase matching condition is modified as $\Delta\delta = \beta(\omega) - \beta(\omega_0) - \beta_1(\omega - \omega_0) - \gamma_0 P_s / 2$. Green curves in Figs. 5(a, b) indicate that phase matching points are exactly the locations of dispersive waves. With frequency related effective area and nonlinear refractive index further included, nonlinear coefficient changes accordingly, and the phase matching condition and spectrum are recalculated as red curves in Figs. 5(a, b). The frequency dependent nonlinear coefficient incurs variations to phase matching condition, blue-shifting the dispersive waves to 680 nm and 2095 nm. Notably there is a third spectral peak except for pump and dispersive waves. The increased nonlinear coefficient at 680 nm enhances the dispersive wave from -34.2 dBm to -18.8 dBm, strong enough to induce another powerful sideband at 2118 nm (peak 3) by degenerate FWM with pump. As illustrated in Fig. 5(c), peak 1 and peak 3 are symmetrical about pump in frequency domain, confirming the origin of peak 3. Based on the device, an octave-spanning frequency comb is generated by LLE-FD. The spectrum spans from 664 nm to 1424 nm (estimated for spectral intensity higher than -60 dBm), reaching visible wavelength range, with extra intense dispersive wave at 2095 nm and dispersive wave sideband at 2118 nm. To our knowledge, this is the first model about micro-combs with full-order frequency dependence of all parameters, which maintains high efficiency under large bandwidth.

4. Conclusions

In conclusion, the LLE-FD is proposed and numerically solved to model micro-comb generation. It is verified to possess high accuracy and computational efficiency, and the theory intrinsically includes full-order frequency dependence of all parameters. To investigate influences of parametric frequency dependence for broadband combs, a SiN micro-ring-resonator with an air slot is carefully designed to achieve octave-spanning combs numerically. Based on the proposed model and device, we get the following conclusions. The frequency related propagation constant will determine whether the dispersive wave is generated, while the frequency dependence of effective area and nonlinear refractive index can induce spectral blue-shift. With the frequency dependence of the three parameters included together, the dispersive wave sideband emerges and this phenomenon has never been reported. The precise prediction of dispersive wave and dispersive wave sideband frequency is beneficial for the f-2f self-referencing. To obtain more accurate solutions in the future, other parametric frequency dependence (such as cavity loss, coupling coefficient) and effects (like Raman scattering) can be easily added like supercontinuum simulations [31]. Our proposed model shows more consistency with actual situations in large bandwidth, provides credible guidance for device design and paves reliable ways for the understanding of micro-combs, especially octave-spanning ones.

References

- [1] P. Del'Haye, A. Schliesser, O. Arcizet, T. Wilken, R. Holzwarth, and T. J. Kippenberg, "Optical frequency comb generation from a monolithic microresonator," *Nature*, vol. 450, no. 7173, pp. 1214–1217, Dec. 2007.
- [2] P. Del'Haye *et al.*, "Phase-coherent microwave-to-optical link with a self-referenced microcomb," *Nature Photon.*, vol. 10, no. 8, pp. 516–520, Aug. 2016.
- [3] S. B. Papp, K. Beha, P. Del'Haye, F. Quinlan, H. Lee, K. J. Vahala, and S. A. Diddams, "Microresonator frequency comb optical clock," *Optica*, vol. 1, no. 1, pp. 10–14, Jul. 2014.
- [4] T. Udem, R. Holzwarth, and T. W. Hänsch, "Optical frequency metrology," *Nature*, vol. 416, no. 6877, pp. 233–237, Mar. 2002.
- [5] E. Obrzud *et al.*, "A microphotonic astrocomb," *Nature Photon.*, vol. 13, no. 1, pp. 31–35, Jan. 2019.
- [6] V. Brasch, E. Lucas, J. D. Jost, M. Geiselmann, and T. J. Kippenberg, "Self-referenced photonic chip soliton Kerr frequency comb," *Light Sci. Appl.*, vol. 6, no. 1, Jan. 2017, Art. no. e16202.
- [7] E. S. Lamb, D. R. Carlson, D. D. Hickstein, J. R. Stone, S. A. Diddams, and S. B. Papp, "Optical-frequency measurements with a Kerr microcomb and photonic-chip supercontinuum," *Phys. Rev. A*, vol. 9, no. 2, Feb. 2018, Art. no. 024030.
- [8] A. J. Scroggie, W. J. Firth, G. S. McDonald, M. Tlidi, R. Lefever, and L. A. Lugiato, "Pattern formation in a passive Kerr cavity," *Chaos, Solitons Fractals*, vol. 4, no. 8/9, pp. 1323–1354, Aug. 1994.
- [9] A. G. Vladimirov, S. V. Gurevich, and M. Tlidi, "Effect of Cherenkov radiation on localized-state interaction," *Phys. Rev. A*, vol. 97, no. 1, Jan. 2018, Art. no. 013816.
- [10] M. H. P. Pfeiffer *et al.*, "Octave-spanning dissipative Kerr soliton frequency combs in Si_3N_4 microresonators," *Optica*, vol. 4, no. 7, pp. 684–691, Jun. 2017.
- [11] A. C. Turner *et al.*, "Tailored anomalous group-velocity dispersion in silicon channel waveguides," *Opt. Express*, vol. 14, no. 10, pp. 4357–4362, May 2006.
- [12] L. Zhang *et al.*, "Generation of two-cycle pulses and octave-spanning frequency combs in a dispersion-flattened micro-resonator," *Opt. Lett.*, vol. 38, no. 23, pp. 5122–5125, Dec. 2013.
- [13] J. Wang *et al.*, "Robust cavity soliton formation with hybrid dispersion," *Photon. Res.*, vol. 6, no. 6, pp. 647–651, Jun. 2018.
- [14] S. Coen, H. G. Randle, T. Sylvestre, and M. Erkintalo, "Modeling of octave-spanning Kerr frequency combs using a generalized mean-field Lugiato–Lefever model," *Opt. Lett.*, vol. 38, no. 1, pp. 37–39, Jan. 2013.
- [15] M. Tlidi *et al.*, "Control and removal of modulational instabilities in low-dispersion photonic crystal fiber cavities," *Opt. Lett.*, vol. 32, no. 6, pp. 662–664, Mar. 2007.
- [16] Y. K. Chembo, D. Gomila, M. Tlidi, and C. R. Menyuk, "Theory and applications of the Lugiato-Lefever Equation," *Eur. Phys. J. D*, vol. 71, p. 299, Nov. 2017.
- [17] T. Hansson, D. Modotto, and S. Wabnitz, "On the numerical simulation of Kerr frequency combs using coupled mode equations," *Opt. Commun.*, vol. 312, pp. 134–136, Feb. 2014.
- [18] Y. K. Chembo, and N. Yu, "Modal expansion approach to optical-frequency-comb generation with monolithic whispering-gallery-mode resonators," *Phys. Rev. A*, vol. 82, no. 3, Sep. 2010, Art. no. 033801.
- [19] M. R. E. Lamont, Y. Okawachi, and A. L. Gaeta, "Route to stabilized ultrabroadband microresonator-based frequency combs," *Opt. Lett.*, vol. 38, no. 18, pp. 3478–3481, Sep. 2013.
- [20] C. Bao, and C. Yang, "Mode-pulling and phase-matching in broadband Kerr frequency comb generation," *J. Opt. Soc. Amer. B*, vol. 31, no. 12, pp. 3074–3079, Dec. 2014.
- [21] S. Wang, H. Guo, X. Bai, and X. Zeng, "Broadband Kerr frequency combs and intracavity soliton dynamics influenced by high-order cavity dispersion," *Opt. Lett.*, vol. 39, no. 10, pp. 2880–2883, May 2014.

- [22] P. V. Mamyshev and S. V. Chernikov, "Ultrashort-pulse propagation in optical fibers," *Opt. Lett.*, vol. 15, no. 19, pp. 1076–1078, Oct. 1990.
- [23] M. H. Frosz, P. M. Moselund, P. D. Rasmussen, C. L. Thomsen, and O. Bang, "Increasing the blue-shift of a supercontinuum by modifying the fiber glass composition," *Opt. Express*, vol. 16, no. 25, pp. 21076–21086, Dec. 2008.
- [24] G. P. Agrawal, *Nonlinear Fiber Optics*. Cambridge, MA, US: Academic Press, 2007
- [25] O. V. Sinkin, R. Holzlochner, J. Zweck, and C.R. Menyuk, "Optimization of the split-step Fourier method in modeling optical-fiber communications systems," *J. Lightw. Technol.*, vol. 21, no. 1, pp. 61–68, May 2003.
- [26] A. A. Rieznik, T. Tolisano, F. A. Callegari, D. F. Grosz, and H.L. Fragnito, "Uncertainty relation for the optimization of optical-fiber transmission systems simulations," *Opt. Express*, vol. 13, no. 10, pp. 3822–3834, May 2005.
- [27] D. Milam, "Review and assessment of measured values of the nonlinear refractive-index coefficient of fused silica," *Appl. Opt.*, vol. 37, no. 3, pp. 546–550, Jan. 1998.
- [28] K. Ikeda, R. E. Saperstein, N. Alic, and Y. Fairman, "Thermal and Kerr nonlinear properties of plasma-deposited silicon nitride/silicon dioxide waveguides," *Opt. Express*, vol. 16, no. 17, pp. 12987–12994, Aug. 2008.
- [29] L. Wang, W. Xie, D. V. Thourhout, Y. Zhang, H. Yu, and S. Wang, "Nonlinear silicon nitride waveguides based on a PECVD deposition platform," *Opt. Express*, vol. 26, no. 8, pp. 9645–9654, Apr. 2018.
- [30] Z. Lu *et al.*, "Deterministic generation and switching of dissipative Kerr soliton in a thermally controlled micro-resonator," *AIP Advances*, vol. 9, no. 2, Feb. 2019, Art. no. 025314.
- [31] J. M. Dudley, G. Genty, and S. Coen, "Supercontinuum generation in photonic crystal fiber," *Rev. Modern Phys.*, vol. 78, no. 4, Oct. 2006, Art. no. 1135.